

## CFD and EnKF coupling estimation of LNG leakage and dispersion

Wu, Jiansong; Cai, Jitao; Yuan, Shuaiqi; Zhang, Xiaole; Reniers, Genserik

**DOI**

[10.1016/j.ssci.2021.105263](https://doi.org/10.1016/j.ssci.2021.105263)

**Publication date**

2021

**Document Version**

Accepted author manuscript

**Published in**

Safety Science

**Citation (APA)**

Wu, J., Cai, J., Yuan, S., Zhang, X., & Reniers, G. (2021). CFD and EnKF coupling estimation of LNG leakage and dispersion. *Safety Science*, 139, Article 105263. <https://doi.org/10.1016/j.ssci.2021.105263>

**Important note**

To cite this publication, please use the final published version (if applicable). Please check the document version above.

**Copyright**

Other than for strictly personal use, it is not permitted to download, forward or distribute the text or part of it, without the consent of the author(s) and/or copyright holder(s), unless the work is under an open content license such as Creative Commons.

**Takedown policy**

Please contact us and provide details if you believe this document breaches copyrights. We will remove access to the work immediately and investigate your claim.

## 1     **CFD and EnKF coupling estimation of LNG leakage and dispersion**

2     **Abstract:** As a kind of clean fuel, increasing quantities of natural gas have been  
3 transported as liquefied natural gas (LNG) worldwide. The safety of LNG storage has  
4 gained the concerns from the public due to the potential severe consequences that may  
5 arise from LNG leakage. In this paper, a three-dimensional model with the combination  
6 of computational fluid dynamics (CFD) and the ensemble Kalman filter (EnKF) is  
7 proposed to predict LNG vapor dispersion and estimate the strength of the LNG leakage  
8 source. The LNG vapor dispersion CFD model is validated by the experimental data  
9 with good feasibility, and is further demonstrated with the reasonable modeling of the  
10 characteristics of the LNG vapor dispersion in a typical receiving terminal. The  
11 effectiveness of the proposed CFD and EnKF coupling model is evaluated and validated  
12 by a twin experiment. The results of the twin experiment indicate that the proposed  
13 CFD and EnKF coupling model allows the integration of observation data into the CFD  
14 simulations to enhance the prediction accuracy of the LNG vapor spatial-temporal  
15 distribution and thereby realizing a reasonable estimation of the LNG leakage velocity  
16 under complex environments. This study can provide technical supports for safety  
17 control, loss prevention and emergency response in case of LNG leakage accidents.

18     **Keywords:** LNG leakage; LNG vapor dispersion; LNG receiving terminal;  
19 computational fluid dynamics; ensemble Kalman filter

1 **CFD and EnKF coupling estimation of LNG leakage and dispersion**

2 Jiansong Wu<sup>a</sup>, Jitao Cai<sup>a</sup>, Shuaiqi Yuan<sup>a,c,\*</sup>, Xiaole Zhang<sup>b</sup>, Genserik Reniers<sup>c</sup>

3 <sup>a</sup> School of Emergency Management & Safety Engineering, China University of Mining and  
4 Technology, Beijing 100083, China;

5 <sup>b</sup> Institute of Environmental Engineering, ETH Zürich, Zürich, CH-8093, Switzerland;

6 <sup>c</sup> Safety and Security Science Group, Faculty of Technology, Policy and Management, TU  
7 Delft, Delft, The Netherlands

8 \*Corresponding author: cumtbyuanshuiqi@163.com

# 1 **CFD and EnKF coupling estimation of LNG leakage and dispersion**

## 2 **1. Introduction**

3       The Liquefied Natural Gas (LNG) industry has attracted a lot of attention in the  
4 past few decades due to the increasing demand for clean energy all over the world. LNG  
5 receiving terminals that are equipped with large cryogenic storage tanks are regarded  
6 as an ideal way to satisfy the energy storage and energy supply ([Lee et al., 2012](#); [Li et  
7 al., 2012](#)). As a kind of flammable and cryogenic gas, leaked LNG vapor could become  
8 a gas cloud rapidly because of the mass heat exchange with the atmospheric  
9 environment. There are possibilities of causing catastrophic consequences induced by  
10 the LNG tank leakage, such as cryogenic burns, fires, explosions, and so on. When  
11 serious LNG leakage accidents occur, the flammable gas cloud that formed by mixing  
12 natural gas and air could be driven by the ambient wind for several kilometers, which  
13 will pose serious threats to the human health and safety, and the environment.  
14 Meanwhile, the leaked LNG vapor will be driven by the negative buoyancy force  
15 because of the low temperature of LNG vapor at the initial stage of LNG leakage, which  
16 will aggravate the dangerous area ([Pontiggia et al., 2009](#)). As a result, the characteristics  
17 of LNG vapor dispersion, the prediction of the LNG vapor distribution and the  
18 estimation of the strength of the leakage source after LNG leakage have been a research  
19 focus in the past decade, which is of great significance for the loss prevention, safety  
20 control and emergency response of LNG leakage accidents.

21 In the early years, there were some studies investigating LNG spill accidents,  
22 which mainly focused on the field tests at relatively open terrains ([Burro Series Data](#)  
23 [Report,1982](#); [Coyote Series Data Report, 1983](#); [Falcon Series Data Report, 1990](#)).  
24 These experiments analyzed the process and characteristics of the LNG spilling on  
25 water and spreading with the ambient wind. Meanwhile, some Computational Fluid  
26 Dynamics (CFD) models have been developed for LNG spilling and dispersion  
27 simulation. Based on Coyote series experiments, Sklavounos et al. presented a  
28 comparison between ANSYS CFX and two popular box-models (SLAB and DEGADIS)  
29 by using statistical performance measures ([Sklavounos et al., 2006](#)). [Cormier et al.](#)  
30 ([Cormier et al., 2009](#)) and [Qi et al. \(Qi et al., 2010\)](#) employed the Brayton Fire Training  
31 Field (BFTF) experimental data to validate the ANSYS CFX code. Then, the process  
32 of LNG leakage and dispersion at a large pit with the consideration of the effects of  
33 dike wall/fence and the sensitivity analysis of several key parameters were investigated  
34 as well. The results indicated that the ANSYS CFX could obtain a good performance  
35 in the simulation of non-isothermal gas dispersion. What's more, the multi-phase of the  
36 LNG leakage process was taken into consideration in the previous studies. [Giannissi et](#)  
37 [al. proposed a two-phase jet model, which could realize the simulation of LNG vapor](#)  
38 [dispersion and LNG liquid pool spreading simultaneously, and the Falcon series](#)  
39 [experiments were selected to validate the proposed two-phase model with good](#)  
40 [reliability \(\[Giannissi et al., 2013\]\(#\)\)](#). Additionally, the ANSYS FLUENT with the  
41 combination of the Lee model was proposed to simulate the LNG multi-phase

42 transformation process, which well predicted the peak value of LNG vapor compared  
43 with the Falcon series experimental data and other numerical models (Luo et al., 2018).  
44 However, the above studies mainly focused on the evaluation of the proposed CFD  
45 models by simplified experiments data without the consideration of the realistic  
46 complex layouts of a real LNG storage site. By contrast, Sun et al. (Sun et al., 2013)  
47 studied the LNG spill accident at an LNG station by using ANSYS FLUENT and  
48 assessed the risk of an LNG spill accident with the consideration of the influence of  
49 dyke walls. Similarly, Guo et al. utilized the Burro series test to evaluate the  
50 applicability of the Fluidyn-PANACHE code, and the effects of the atmosphere stability  
51 on the LNG vapor dispersion were discussed (Guo et al., 2019). Baalisampanga et al.  
52 (Baalisampanga et al., 2019) and Dasgotra et al. (Dasgotra et al., 2018) studied the LNG  
53 spilling accident using FLACS considering its cascading consequences, and the results  
54 showed that the integrated consequences were more severe.

55         However, there are always some uncertainties about the parameters of the LNG  
56 leakage source and dispersion process, which could bring a certain degree of errors to  
57 the simulation results. The LNG leakage rate and the ambient wind speeds under  
58 complex environments are difficult to estimate, which could result in a large deviation  
59 between simulation results and the real situations. Moreover, the estimation of LNG  
60 vapor leakage rate is of significance to provide technical supports for emergency  
61 response. The estimation of hazardous materials leakage source has been investigated  
62 by many studies. The data assimilation (DA) method is proven with good reliability

63 and practicability to estimate the strength of the leakage source and predict the  
64 hazardous materials spatio-temporal distribution (Zhang et al., 2014; Xue et al., 2018;  
65 Wu et al., 2018; Yuan et al., 2019). As a kind of sequential DA method, the ensemble  
66 Kalman filter (EnKF) method is widely used in the prediction of hazardous materials  
67 dispersion and with good feasibility to reconstruct hazardous materials release source  
68 by integrating observation data into the dispersion models (Zhang et al., 2014; Yuan et  
69 al., 2019). These studies demonstrate that the DA method and the ensemble Kalman  
70 filter have great potentials in the prediction of LNG vapor dispersion and to realize the  
71 estimation of the strength of the LNG vapor leakage source.

72 In this study, a three-dimensional [CFD and EnKF coupling model](#) is proposed to  
73 estimate the LNG leakage and predict the LNG dispersion process. An OpenFOAM  
74 solver is improved to simulate the LNG vapor dispersion process, and the EnKF method  
75 is used to integrate the observation data into the OpenFOAM simulations and realize  
76 the estimation of the leakage source at the same time. Firstly, the OpenFOAM solver  
77 for simulating LNG vapor dispersion was evaluated and validated by using the Burro 8  
78 spill test data. Furthermore, scenario analysis of LNG vapor leakage in an LNG  
79 receiving terminal located in the north of China is conducted to investigate the  
80 characteristics of LNG vapor dispersion in complex environments. Finally, a twin  
81 experiment is done to evaluate and validate the proposed [CFD and EnKF coupling](#)  
82 [model](#) through quantitative and qualitative analysis. This study could be helpful to  
83 provide technical supports for safety control and emergency response of LNG leakage

84 accidents.

## 85 **2. Methodology**

### 86 **2.1 Governing equations of LNG vapor dispersion**

87 In this study, a three-dimensional compressible Navier-Stokes solver based on  
88 OpenFOAM is employed to simulate LNG vapor leakage and dispersion. This solver  
89 has been validated with feasibility and effectiveness in the simulation of gravity-driven  
90 gas flows (Fiates et al., 2016; Mack and Spruijt, 2013). In this paper, only the mass  
91 conservation equation, momentum conservation equation and no-reaction species  
92 mass-conservation equation are utilized, because there is no chemical reaction during  
93 the LNG vapor leakage and dispersion process. The basic governing equations of LNG  
94 vapor dispersion can be expressed as follows:

95 (i) Mass conservation equation

$$96 \quad \frac{\partial \rho}{\partial t} + \nabla \cdot (\rho \mathbf{v}) = 0 \quad (1)$$

97 (ii) Momentum conservation equation

$$98 \quad \frac{\partial}{\partial t}(\rho \mathbf{v}) + \nabla \cdot (\rho \mathbf{v} \mathbf{v}) = -\nabla p + \nabla \tau + \rho \mathbf{g} + \mathbf{F} \quad (2)$$

99 (iii) Species mass-conservation equation

$$100 \quad \frac{\partial}{\partial t}(\rho Y_i) + \nabla \cdot (\rho \mathbf{v} Y_i) = \nabla \cdot (D_c \nabla (\rho Y_i)) + S_i \quad (3)$$

101 where  $\rho$  is the density of the mixed gas,  $\mathbf{v}$  is the velocity,  $p$  presents the pressure, and  
102  $\tau$  is the shear stress, which can be calculated according to the law of viscosity.  $\mathbf{g}$  and



103  $\mathbf{F}$  present the gravity acceleration and the external forces respectively, and  $Y_i$   
 104 represents the volume concentration of different species.  $D_c$  represents the diffusion  
 105 coefficient reflecting the gas diffusion degree and  $S_i$  represents the generalized source  
 106 term.

## 107 2.2 Turbulence Model

108 The typical  $\kappa$ - $\varepsilon$  turbulence model is widely applied in the CFD simulation of gas  
 109 dispersion due to its stability and accurate prediction (Liu et al., 2018; Siddiqui et al.,  
 110 2012). However, the standard  $\kappa$ - $\varepsilon$  turbulence model has some shortages in handling  
 111 fluid on the curved surface or even more complex flows. Therefore, the SST turbulence  
 112 model was employed in this study that is a promising turbulence model in the  
 113 simulation of gravity-driven gas flow with the combination of the advantages of the  
 114 standard  $\kappa$ - $\varepsilon$  model and the  $k$ - $\omega$  model (Li et al., 2016; Xing et al. 2013). The solved  
 115 equations of the SST turbulence model are presented as follows:

$$116 \quad \frac{\partial(\rho k)}{\partial t} + \nabla \cdot (\rho U k) = \nabla \cdot \left[ \left( u + \frac{u_t}{\sigma_\omega} \right) \nabla k \right] + P_k - \beta' \rho k \omega \quad (4)$$

$$117 \quad \frac{\partial(\rho \omega)}{\partial t} + \nabla \cdot (\rho U \omega) = \nabla \cdot \left[ \left( u + \frac{u_t}{\sigma_\omega} \right) \nabla \omega \right] + \frac{\alpha \omega}{k} P_k - \beta \rho \omega^2 \quad (5)$$

$$118 \quad \mu_t = \frac{\rho k}{\omega} \quad (6)$$

119 In the equations above,  $\beta'$ ,  $\alpha$ ,  $\sigma_k$ ,  $\sigma_\omega$ , and  $\beta$  are the model constants, which are assigned  
 120 as  $\beta' = 0.09$ ,  $\alpha = \frac{5}{9}$ ,  $\sigma_k = \sigma_\omega = 2$ ,  $\beta = 0.075$  respectively according to a previous  
 121 study (Sklavounos et al., 2006).  $\kappa$  means kinetic viscosity,  $\omega$  represents the turbulent  
 122 frequency, and  $P_k$  is the production rate of the turbulence.  $u_t$  represents turbulent

123 kinetic that can be calculated by using equation (6).

### 124 **2.3 Ensemble Kalman Filter**

125 The ensemble Kalman filter (EnKF) is a kind of widely-used data assimilation  
126 method, which can deal with the prediction of nonlinear dynamic models. It has some  
127 obvious advantages, such as consistent estimation of spatiotemporally varying model  
128 covariance, ease of implementation, and estimation of the posterior error (Pu and  
129 Hacker, 2009). The EnKF method has been widely used for solving many engineering  
130 problems, typically, it has already been successfully applied in the hydrological model  
131 prediction (Pu and Hacker, 2009; Valdes-Abellan et al., 2018), forecasting of smoke  
132 movement during tunnel fires (Ji et al., 2018), prediction of the indoor environment  
133 (Lin and Wang, 2013) and gas release and dispersion in an underground tunnel (Wu et  
134 al., 2018; Yuan et al., 2019). Meanwhile, the [CFD and EnKF coupling model](#) is also an  
135 alternative way to provide supports for the emergency of the nuclear accident (Zhang  
136 et al., 2015a; Zhang et al., 2015b).

137 In this study, the basic formulas of EnKF are described as follows:

$$138 \quad y^f(t_i) = D \left( y^f(t_{i-1}) \right) \quad (7)$$

$$139 \quad y^a(t_i) = y^f(t_i) + E \left( r(t_i) - L \left( y^f(t_i) \right) \right) \quad (8)$$

140 Where  $y$  denotes the state vector,  $t_i$  and  $t_{i-1}$  represent the time step,  $y^f(t_i)$  is the  
141 predicted value at time  $t_i$ ,  $y^a(t_i)$  is the analytical value at time  $t_i$ ,  $D$  and  $L$  mean the  
142 nonlinear dynamic system model and the observation model respectively.  $r$  means the

143 observation vector and  $E$  denotes the ensemble Kalman gain.

144 EnKF describes the nonlinearity of the dynamic system by using a set of state

145 estimations. The state matrix is generated as follows:

$$146 \quad Y = \frac{1}{\sqrt{M-1}} (y_1, y_2, \dots, y_M) \quad (9)$$

$$147 \quad Y' = \frac{1}{\sqrt{M-1}} (y_1 - \bar{y}, y_2 - \bar{y}, \dots, y_M - \bar{y}) \quad (10)$$

$$148 \quad Q_e = Y'Y'^T \quad (11)$$

149 Where  $Y$  represents the state matrix,  $M$  is the ensemble size.  $Q_e$  denotes the ensemble

150 covariance matrix, which is generated by the state ensemble. The ensemble Kalman

151 gain and the prediction of the observation vector are calculated as follows:

$$152 \quad r^f = L(y^f) \quad (12)$$

$$153 \quad E = Q_e^f L^T (L Q_e^f L^T + Z_e)^{-1} \quad (13)$$

154 Where  $r^f$  means the prediction of the observation vector, and  $Z_e$  denotes the

155 observation ensemble covariance matrix, which can be given as follows:

$$156 \quad R = (r_o + \varepsilon_1 \dots r_o + \varepsilon_n \dots r_o + \varepsilon_M) \quad (14)$$

$$157 \quad R' = (\varepsilon_1 \dots \varepsilon_n \dots \varepsilon_M) \quad (15)$$

$$158 \quad Z_e = R'R'^T \quad (16)$$

159 Where  $\varepsilon_n$  is the pseudo-random perturbation.  $R$  indicates an ensemble of observation,

160 which can be obtained by adding  $\varepsilon_n$  to the observation data  $r_o$ .  $Z_e$  represents the

161 covariance matrix of  $R'$ .

## 162 2.4 State vector and update of source term

163 In this paper, the state vector consists of the LNG vapor concentrations and the  
164 leakage velocities:

$$165 \quad y = (c_1 \dots c_i \dots c_n \quad l_1 \dots l_j \dots l_m)^T \in R^{n+m} \quad (17)$$

166 Where  $y$  denotes the state vector,  $c$  means the concentration of the LNG vapor and  $l$   
167 means the LNG vapor leakage velocity at the leak hole. The subscript  $n$  and  $m$  represent  
168 the number of LNG vapor concentrations and the number of data assimilation time steps  
169 respectively.

$$170 \quad l_j^b = \sum_{i=1}^N l_{j-1}^a(i) / M \quad (18)$$

$$171 \quad l_j^f(i) = l_j^b + \delta l_j^b(i), \quad i = 1, 2, \dots, M \quad (19)$$

172 Where  $l_{j-1}^a$  means the latest updated leakage velocity ensemble,  $i$  and  $M$  represent the  
173 ensemble member and ensemble size respectively. The ensemble  $l_1^f$  is the first-guess  
174 leakage velocity, which can be initialed by the users.  $l_j^f$  represents a prior gas leakage  
175 velocity for the  $j$ -th data assimilation, which are automatically calculated according to  
176 the formulas (19). The added noise  $\delta l_j^b(i)$  is generated as follows:

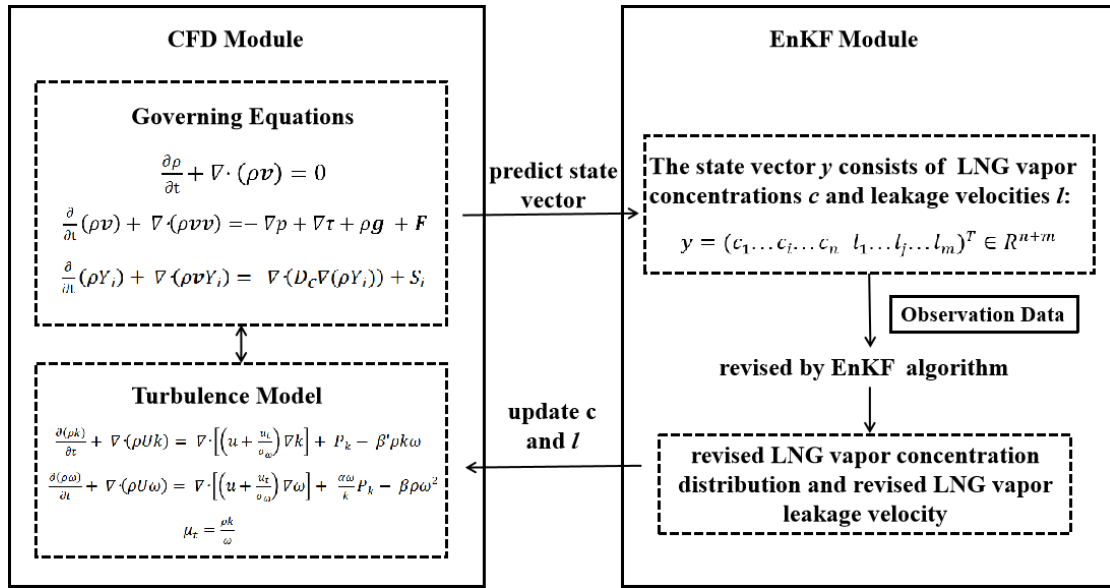
$$177 \quad \delta l_j^b(i) = \alpha \delta l_{j-1}^a(i) + \sqrt{1 - \alpha^2} c_j(i) \sigma_{j-1}^a, \quad i = 1, 2, \dots, M \quad (20)$$

178 Where  $\delta l_{j-1}^a(i)$  denotes the deviation between the  $i$ -th analysis leakage velocity  
179 and the ensemble mean  $\sigma_{j-1}^a$  represents the standard deviation, which is calculated by

180  $l_{j-1}^a$ .  $c_j(i)$  is random numbers, which following the Gaussian distribution  $N(0,1)$ . The  
 181 parameter  $\alpha$  (range from 0 to 1) controls the degree to which the influence of the prior  
 182 state will be retained, which can be set as 0.99 in this paper.

183 **2.5 CFD and EnKF coupling model for leakage source estimation and dispersion**  
 184 **prediction**

185 With the combination of LNG vapor dispersion model and EnKF algorithm, the  
 186 **CFD and EnKF coupling model** for LNG vapor leakage source estimation and  
 187 dispersion prediction are developed by the procedure shown in **Fig. 1**.



188  
 189 Fig. 1 Framework of the **CFD and EnKF coupling model** for LNG vapor leakage  
 190 source estimation and dispersion prediction

191 The **CFD and EnKF coupling model** for leakage source estimation and dispersion  
 192 prediction consists of the CFD module and the EnKF module. The CFD module is  
 193 operated to simulate the LNG vapor dispersion process through the calculations of

194 governing equations and turbulence model. Meanwhile, the state vector of the EnKF  
195 module, which consists of LNG vapor concentrations and the leakage velocities in the  
196 leak hole can be predicted by the CFD module calculation. When the observation data  
197 is available, the state vector can be revised by the EnKF algorithm and the updates of  
198 the LNG vapor concentrations and the LNG vapor leakage velocities can be realized.  
199 Finally, the revised LNG vapor concentration distribution and the revised LNG vapor  
200 leakage velocity will be utilized into the CFD module for the next calculation of LNG  
201 vapor dispersion and a data assimilation step is finished.

### 202 **3. Results and discussion**

203 This section is organized as follows: Firstly, as a coupling model consisting of the  
204 CFD model and the EnKF algorithm, the feasibility of the CFD and EnKF coupling  
205 model can only be guaranteed after the validation of the CFD model. Therefore, the  
206 OpenFOAM-based CFD model was evaluated by experimental data firstly and then a  
207 case study was investigated as well to analyze the basic characteristics of the LNG  
208 vapor dispersion. Finally, the effectiveness of the proposed CFD and EnKF coupling  
209 model was demonstrated by a twin experiment.

#### 210 **3.1 Evaluation and validation of OpenFOAM code**

211 As a kind of open-source CFD computing platform, OpenFOAM gained  
212 popularity in engineering system and scientific research. However, it has not been  
213 validated in a specific scenario associated with an LNG spill and vapor dispersion.

214 Moreover, the validation of the OpenFOAM code in the simulation of LNG vapor  
215 leakage and dispersion is of significance to the development of the [CFD and EnKF](#)  
216 [coupling model](#) LNG vapor leakage and dispersion prediction model, and it is also  
217 beneficial to provide an alternative tool for the investigation of LNG leakage and  
218 dispersion by numerical simulations. In this paper, the experimental data, the results of  
219 ANSYS FLUENT code and the results of the OpenFOAM code will be compared to  
220 validate the applicability of the OpenFOAM simulations.

### 221 3.1.1 Numerical configurations

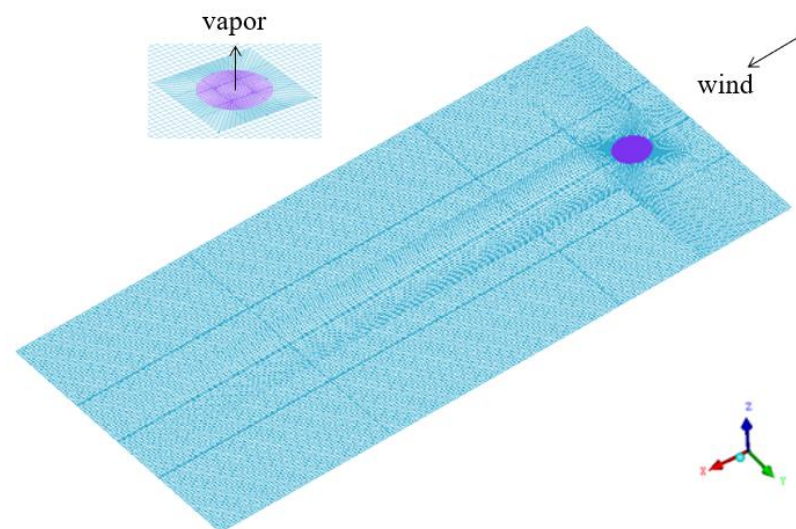
222 The Burro 8 spill test performed by the Lawrence Livermore National Laboratory  
223 (LLNL) at the Naval Weapons Center was considered appropriate enough to investigate  
224 the behaviors and the characteristics of the LNG vapor dispersion due to its stable  
225 atmospheric conditions ([Sun et al., 2013](#)). In the Burro 8 test, the LNG vapor spread  
226 from a pond with a diameter of 58 m into the atmosphere environment. There were 25  
227 gas sensor sites arranged downwind from the center of pond. 20 wind-filed station were  
228 placed in both upwind and downwind to capture the wind velocity and the wind  
229 directions. The experimental setup and the meteorological data involved in the Burro 8  
230 experiment are listed in **Table.1**.

231 Table 1 Experimental setup and meteorological data involved in the Burro 8  
232 experiment

Parameters	values
Spill volume (m <sup>3</sup> )	28.4

Spill duration (s)	107
Spill rate (m <sup>3</sup> /min)	16
Wind speed (m/s)	1.8
Ambient Temperature (°C)	33.1
Relative humidity	4.5 %
Atmospheric stability class	E
Monin-Obukhov length (m)	16.5

233 The computational domain used in the OpenFoam simulation was  
 234 1000\_m×500\_m×50\_m. ANSYS ICEM was employed to create and discretize the  
 235 computational domain. The hexahedral cells with refined mesh close to the pond and  
 236 ground were used and the mesh in the computational domain can be seen in **Fig.2**.



237

238

Fig.2 Mesh in the computational domain

239

240

241

According to the previous studies (Luo et al., 2018; Zhang et al., 2015), the boundary condition of velocity in the wind inlet was prescribed as uneven velocity inlet, which was calculated as follows:



242 
$$U(z) = u_0 \times \left(\frac{z}{z_0}\right)^\lambda \quad (21)$$

243 where  $U(z)$  is the wind velocity at the specific height  $z$ , and  $u_0$  is the reference velocity  
244 at the reference height  $z_0$ . In the Burro 8 test,  $u_0$  was set as 1.8 m/s and  $z_0$  was 2 m.  $\lambda$  is  
245 a dimensionless parameter determined by the atmospheric stability and the surface  
246 roughness, which was set as 0.12 in this study. This uneven velocity inlet was added  
247 into the OpenFOAM simulation by the codeFixedValue function in the OpenFOAM  
248 platform.

249 Due to the rapid evaporation phenomenon when LNG is spilt on a water pond area,  
250 the leakage velocity of the LNG vapor can be calculated by the formula as follows:

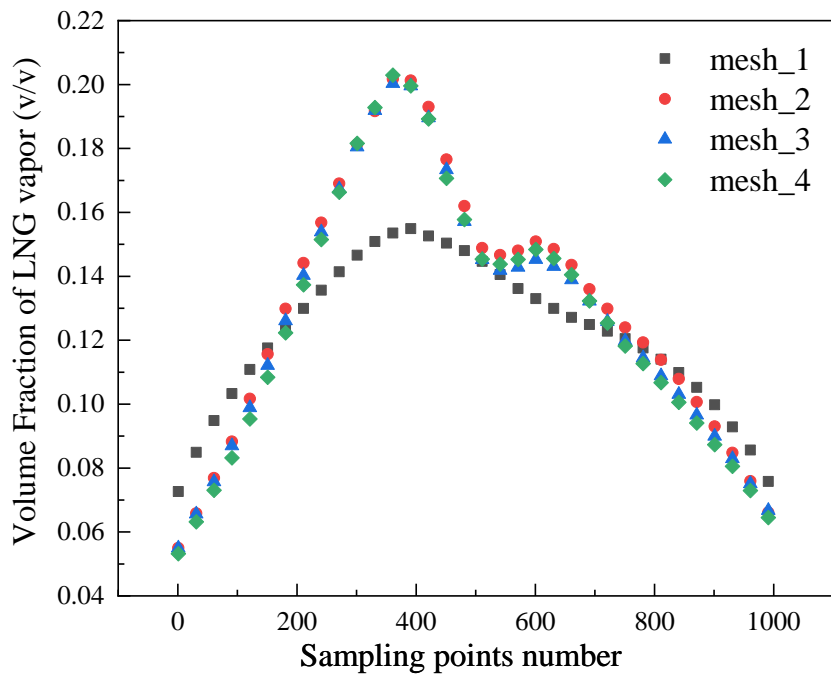
251 
$$U_g = (\rho U)_{liq} / \rho_g, \quad (22)$$

252 Where  $U_g$  is the vapor leakage velocity in the computational domain,  $\rho_{liq}$  and  $\rho_g$  are  
253 the LNG density (424.1 kg/m<sup>3</sup>) and the vapor density (1.76 kg/m<sup>3</sup>) at 111 K respectively.  
254  $U_{liq}$  represents LNG spill velocity, which can be calculated by the spill rate and the  
255 pond diameter.

256 The outflow boundary at 900 m downwind from the origin was set as pressure  
257 outlet, the top and the two sides of the computational domain were assumed far away  
258 from the vapor leakage area, which were set as symmetry boundary conditions. The  
259 ground was set as the wall with no-slip condition. Additionally, all the boundary  
260 conditions applied in the ANSYS FLUENT simulation were set according to the  
261 boundary conditions used in the OpenFOAM simulation.

### 262 3.1.2 Comparison and analysis

263 In order to obtain the mesh-independent simulation results, the mesh independence  
264 analysis was investigated by using four different meshes with grid numbers of 400  
265 thousand, 550 thousand, 700 thousand and 850 thousand. Some sampling points  
266 obtained from a sampling line were selected to perform this mesh sensitivity analysis.  
267 The results of the calculated volume fraction of the LNG vapor at the sampling points  
268 by using four different meshes are shown in **Fig.3**. With the comparison between the  
269 results calculated by a different mesh, the average relative error and max error between  
270 mesh\_1 and mesh\_2 are 0.12 and 0.31 respectively. However, the average relative error  
271 and max error between mesh\_2 and mesh\_3 are 0.023 and 0.045 while 0.018 and 0.042  
272 for mesh\_3 and mesh\_4. Therefore, mesh\_2 was selected for the following simulation  
273 with both good accuracy and less computation load.



274

275

Fig.3 LNG vapor volume fraction at sampling line

276

**Fig.4** presents the horizontal concentration distribution of the LNG vapor at the

277

height of 1 m after LNG spilling. It shows the LNG vapor contours of 1%, 2%, 5%,

278

10%, 15%, 25%, and 35% volume fraction. The results show that a gravity-driven gas

279

cloud moved downwind as time goes by under the stable atmosphere stability in the

280

Burro 8 test. Furthermore, the shapes of the gas cloud obtained from the field test have

281

less symmetry about the center-line of the computational domain compared with the

282

simulation results. The reason for this may be that there was a non-uniform wind speed

283

in different directions existing in the field test, which was ignored in the CFD

284

simulations. However, the lateral and downwind range of the vapor dispersion of the

285

OpenFOAM code results was in a good agreement with the field test and the ANSYS

286

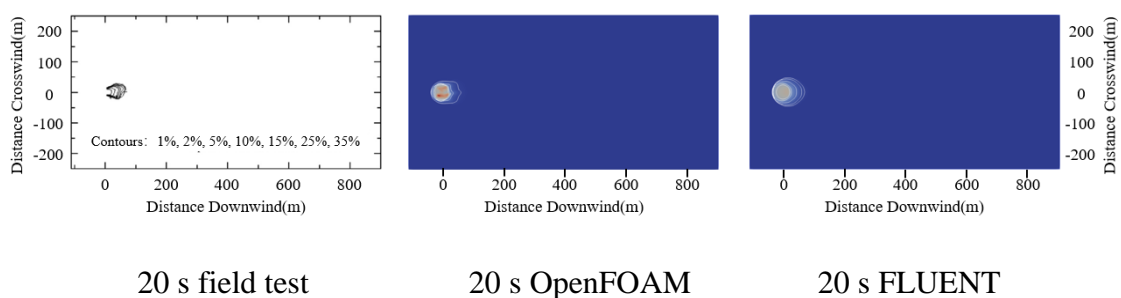
FLUENT simulation, which demonstrates that the OpenFOAM code well reproduced

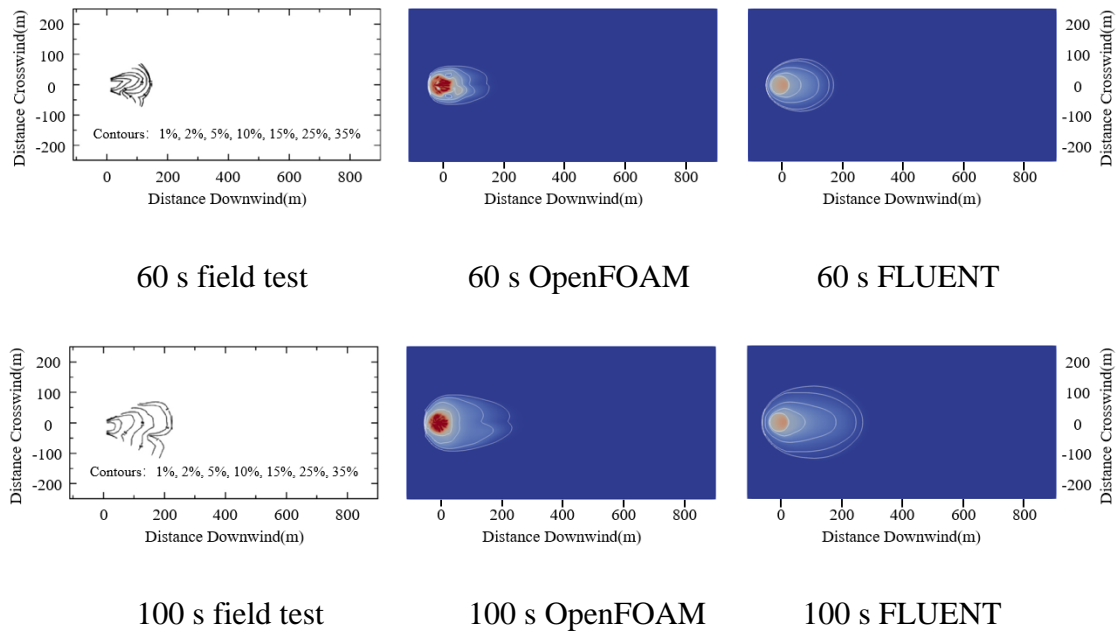
287

the distribution of the LNG vapor dispersion and can be used as an alternative tool for

288

LNG vapor dispersion with good reliability.





289 Fig.4 LNG vapor contours at olume fraction of 1%, 2%, 5%, 10%, 15%, 25%, and  
 290 35%

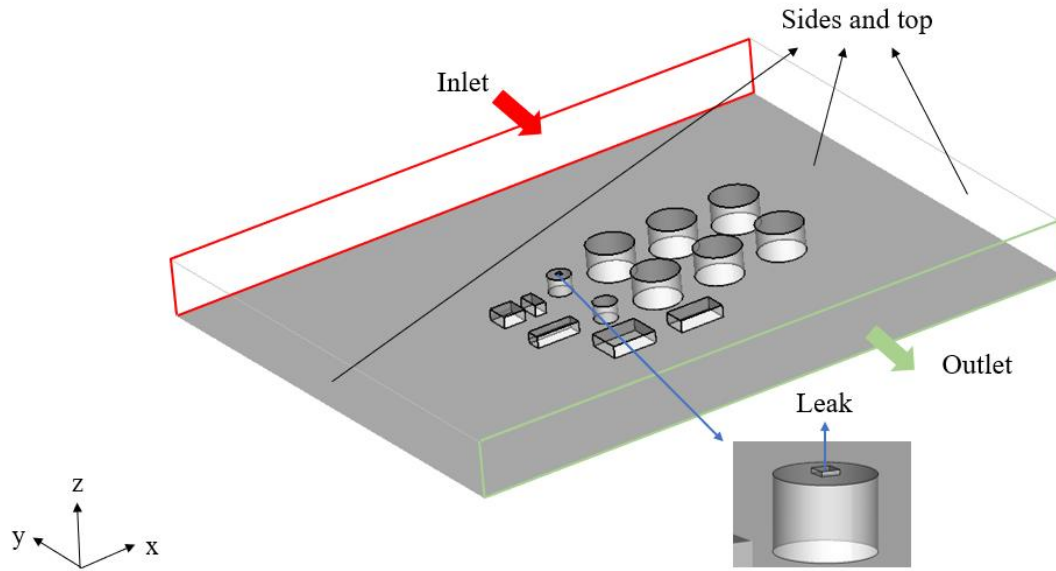
### 291 3.2 LNG vapor dispersion in receiving terminal

292 Different from the experimental data investigated above, the LNG vapor  
 293 dispersion process in the LNG receiving terminal will be influenced by complex  
 294 obstacle layouts, ambient ventilation conditions, buoyancy forces and so on. In order to  
 295 investigate the LNG vapor cloud dispersion in receiving terminal at ports, a typical  
 296 LNG receiving terminal located in the north of China was selected as simulation  
 297 scenario in this section.

#### 298 3.2.1 Numerical configurations of LNG port model

299 In this section, the computational domain has a dimension of  
 300 1120\_m×880\_m×100\_m, and the leakage hole is placed at the center of the  
 301 computational domain. The layout and the boundary conditions of the investigated

302 LNG receiving terminal model are shown in **Fig.5**. Meanwhile, the detailed parameters  
 303 of the LNG receiving terminal model are presented in **Table.2**.



304

305 Fig.5 The layout and boundary conditions of the investigated LNG receiving  
 306 terminal at ports

307

Table 2 Configurations of the investigated LNG receiving terminal model

Parameter	value
Width (m)	220
Height (m)	50
Length (m)	280
Average flow speed in inlet (m/s)	8
Leakage area (m <sup>2</sup> )	64
Leakage velocity of LNG (m/s)	15
Location of leakage source (m)	(500 m, 20 m, 32 m)
Environment temperature (K)	298
Density of LNG at the leak hole (kg/m <sup>3</sup> )	1.76

308 The computational domain above was created and discretized by using ANSYS  
309 ICEM. Three meshes with different grids (20 thousand, 40 thousand, and 60 thousand)  
310 were used for primary simulations and comparisons. It showed that there was a small  
311 average relative error that was 0.048 between the results of mesh\_2 with 40 thousand  
312 grids and mesh\_3 with 60 thousand grids. However, the errors between the results of  
313 mesh\_2 and mesh\_1 with 20 thousand grids can not be ignored, being 0.20. Therefore,  
314 mesh\_2 was selected for the following simulations with better accuracy and computing  
315 speed. Moreover, a wind field under steady-state was calculated and initialed in the  
316 simulation of LNG vapor leakage and dispersion in the LNG receiving terminal in order  
317 to ensure a more realistic leakage scenario.

318 The boundary conditions applied in the simulation are shown as follows:

319 ( i ) Inlet: A power law correlation velocity was utilized in the air inlet boundary,  
320 which was calculated by formula (21). And the  $z_0$  and  $u_0$  were set as 3 m/s and 2 m  
321 respectively according to the meteorological records of northern China. Additionally,  
322 the  $\lambda$  was set as 0.4 with consideration of the layout of the complex buildings.

323 ( ii ) Leak: The leakage velocity of the LNG vapor was set as 15 m/s under the  
324 assumption that the LNG was easy to evaporate and accumulate in the higher part of  
325 the storage tank. The temperature of the leaked LNG vapor at the leak hole was set as  
326 111 K.

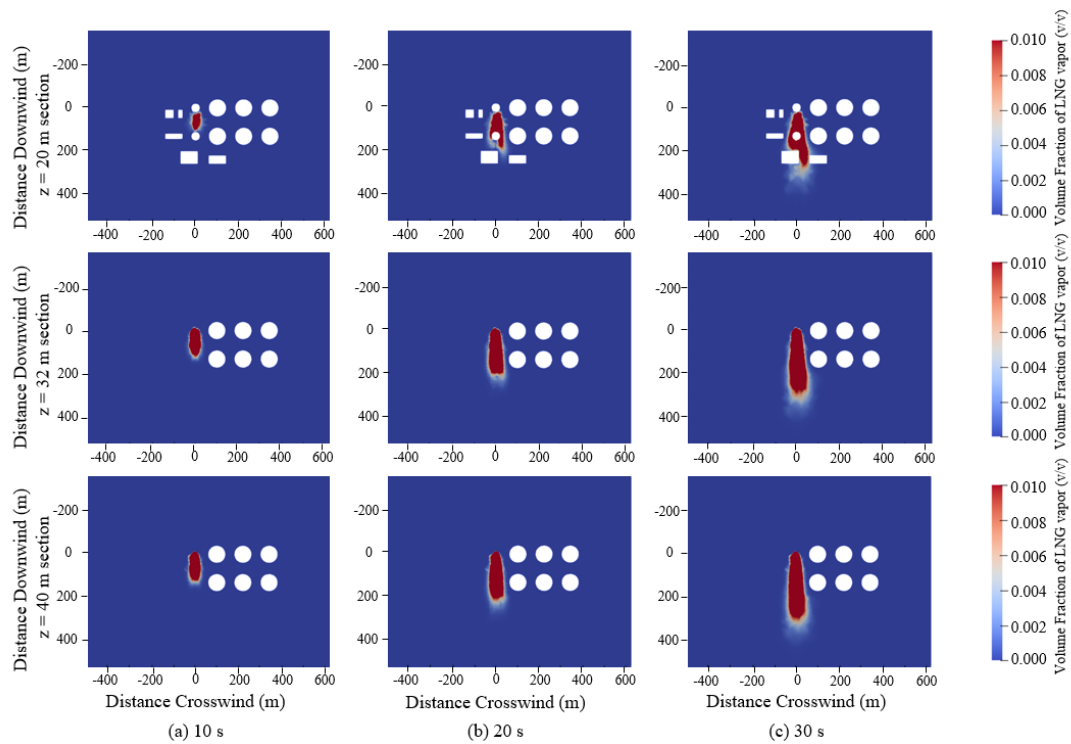
327 (iii) Outlets: The fully developed condition was employed in the outlets as outflow  
328 conditions.

329 (iv) Sides and top: Two sides and the top of the computational domain were  
330 defined as symmetry conditions.

331 (v) Walls: All the walls and blocks in the investigated model were set as no-slip  
332 wall conditions.

### 333 **3.2.2 LNG vapor dispersion analysis**

334 The simulation of LNG vapor leakage and dispersion in the LNG receiving  
335 terminal at ports was presented to investigate the characteristics of the LNG cloud  
336 dispersion. Due to the high molecular weight, the low temperature, and the presence of  
337 the aerosols, some released materials usually have the density that is heavier than the  
338 ambient gas and will be driven by the gravity (Pontiggia et al., 2009). The LNG vapor  
339 usually leaked and dispersed as dense gas at the initial stage before the temperature rose  
340 because of the cryogenic storage condition. However, with the exchange of heat  
341 between leaked LNG vapor and the surrounding atmospheric environment, the leaked  
342 LNG vapor will be heated and behave like light gas gradually. Therefore, the leakage  
343 and dispersion process of the LNG vapor is complex, especially in the environment  
344 with some obstacles, which increases the complexity of the airflow. In this section, the  
345 horizontal and vertical distributions of the LNG vapor are presented in **Fig.6** and **Fig.7**.



346

347

348

Fig.6 Horizontal concentration distribution of LNG vapor at Z=20 m, Z=32 m and Z=40 m sections

349

350

351

352

353

354

355

356

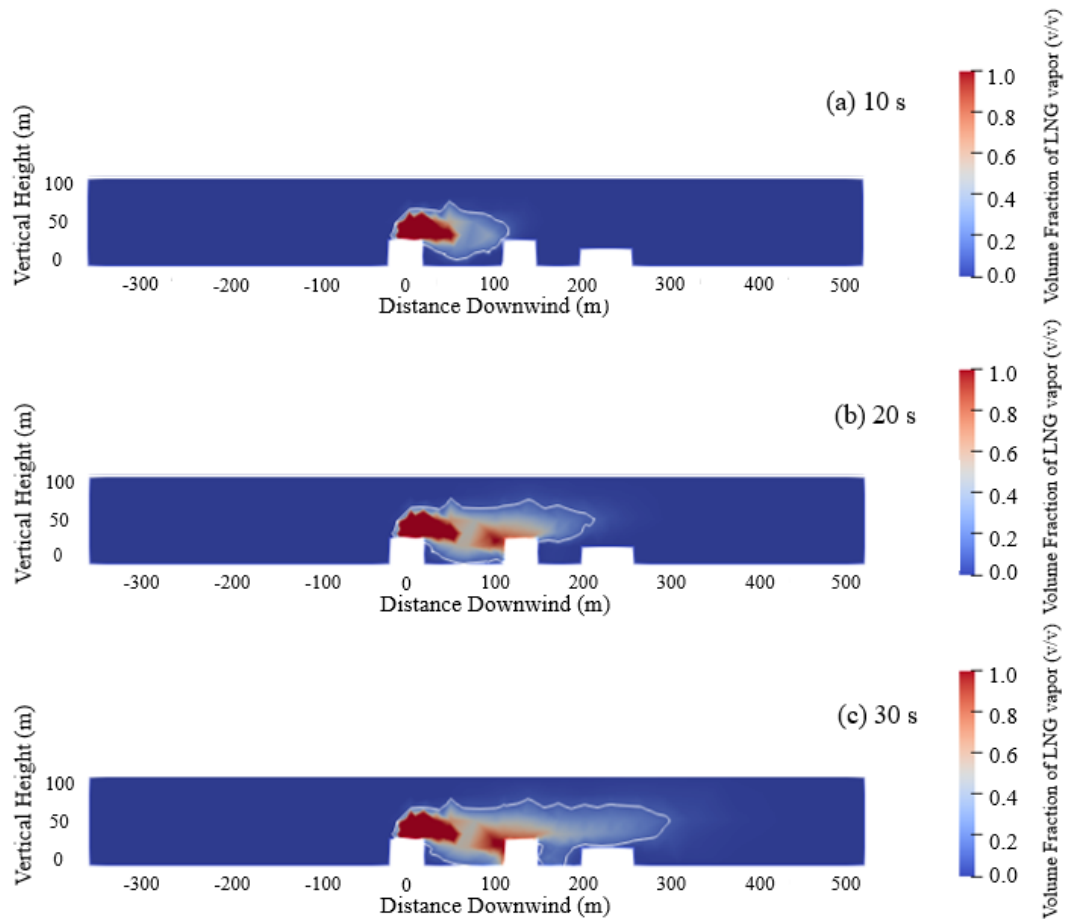
357

358

**Fig.6** compares the horizontal concentration distributions of the LNG vapor at different horizontal section heights (Z=20 m, Z=32 m and Z=40 m) at 10 s, 20 s and 30s. The range of the leaked LNG vapor in the Z=20 m section was smaller than the Z=32 m and Z=40 m sections due to the delay of the LNG vapor dispersion, lower ambient wind speed and the complex obstacles. Since the effects of the obstacles could lead to a low wind velocity at the leeward side of the storage tank, there was an obvious low concentration region at 150 m downwind in the Z=20 m section at 20 s and 30 s. Whereas, the LNG vapor cloud in the Z=32 m and Z=40 m sections had similar range areas because the there was no obstacle that could influence the process of vapor cloud dispersion in the direction of wind flow. Moreover, the vapor cloud range of the z=40



359 m section was slightly greater than  $z=32$  m section, and it was probably because the  
360 applied pow law correlation inlet made a relatively higher wind velocity in the  $z = 40$   
361 m section.



362  
363 Fig.7 Vertical concentration distribution of LNG vapor at X=500 m section

364 The concentration distributions of the LNG vapor in vertical section were  
365 presented in the **Fig.7**. At the initial stage of LNG vapor leakage, the vapor cloud  
366 dispersion was mainly dominated by the leakage velocity and the wind speed near the  
367 leakage source, and then the cryogenic dense vapor cloud affected by the gravity had  
368 the tendency to sink as shown in panel (a). After spreading out of leakage source area,

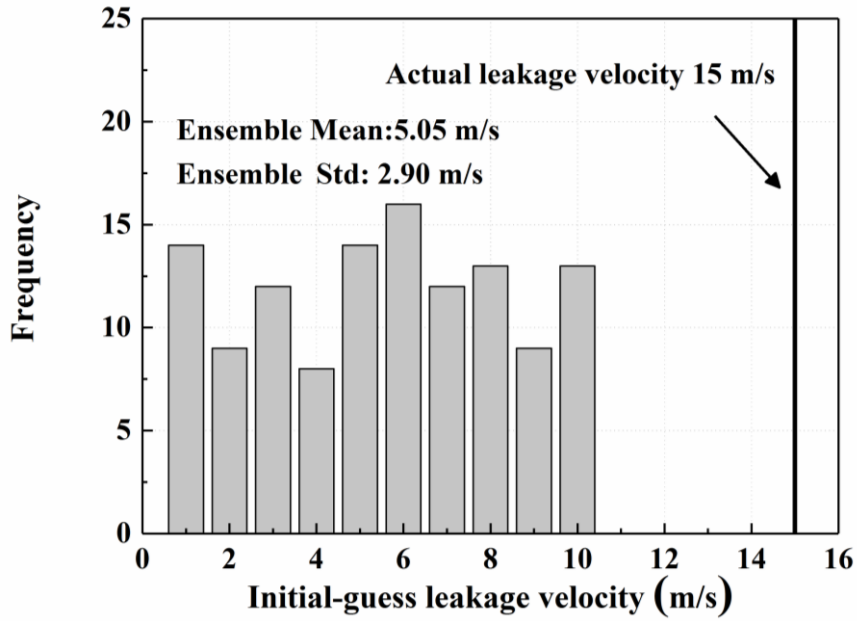
369 the buoyant force and the obstacles would have more influence on the vapor cloud  
370 dispersion gradually. A conspicuous dipped trajectory of vapor cloud could be seen  
371 between the first two tanks and a certain amount of LNG vapor sank into the cavity area  
372 in panel (b) and panel (c). A relatively high concentration of LNG vapor could be seen  
373 near the top of the second tank at 100 m downwind in panel (b) and panel (c). That was  
374 because there were vortexes in the cavity area between the two tanks caused by the  
375 LNG receiving terminal layout, and the similar phenomenon of vapor cloud dispersion  
376 could be seen in the street canyons (Liu et al., 2018). The LNG vapor cloud continued  
377 to spread to around 300 m downwind without obvious sinking trend, it was probably  
378 because the density of the LNG vapor decreased gradually with the heat transfer  
379 between LNG vapor cloud and the atmospheric environment. Therefore, the vapor  
380 cloud dispersion process became momentum-dominated after 300 m downwind in  
381 panel (c).

### 382 **3.3 CFD and EnKF coupling estimation of LNG leakage and dispersion**

383 In this paper, the twin experiment was used to validate the proposed CFD and  
384 EnKF coupling prediction model for LNG vapor leakage and dispersion. Twin  
385 experiment was widely used in the evaluation of data assimilation models (Bengtsson  
386 et al., 1981, Ngodock and Carrier, 2013). There is always a control group in the twin  
387 experiment, in which the numerical simulations with controlled initial parameters can  
388 be used and the simulation of section 3.2 was employed as the control group in this  
389 paper.

### 390 3.3.1 Configurations of the CFD and EnKF coupling model

391 In the CFD and EnKF coupling model, the observation sampling time step was set  
392 as 0.5 s, which means the observation data from the control group will be utilized for  
393 data assimilation every 0.5 s. We set up 100 observation sites in the control group  
394 simulation to obtain observation data of the LNG vapor concentration. The ensemble  
395 size in the CFD and EnKF coupling model was set as 120 and the inflation factor  
396 (Anderson, 2007) was set as 1.0 in this paper. Additionally, two parameters with  
397 uncertainties were taken into account in the proposed model: the initial-guess leakage  
398 velocity and the airflow velocity in the computational domain. We set the initial-guess  
399 leakage velocity as an ensemble following uniform distribution from 0 m/s to 10 m/s,  
400 whereas the actual leakage velocity was 15 m/s, which is shown in Fig. 8. The u  
401 ensemble calculated in the CFD and EnKF coupling model was presumed to follow a  
402 normal distribution of  $N(1, 0.1)$ . We selected 100 observation sites in three sections of  
403 the computational domain, 9 observation sites in the Z=20 m section, 70 observation  
404 sites in the Z=32 m section and 21 observation sites in the X=500 m section respectively.  
405 The layouts of the observation sites are shown in Fig. 9. The detailed configurations of  
406 the CFD and EnKF coupling model are shown in Table 3.

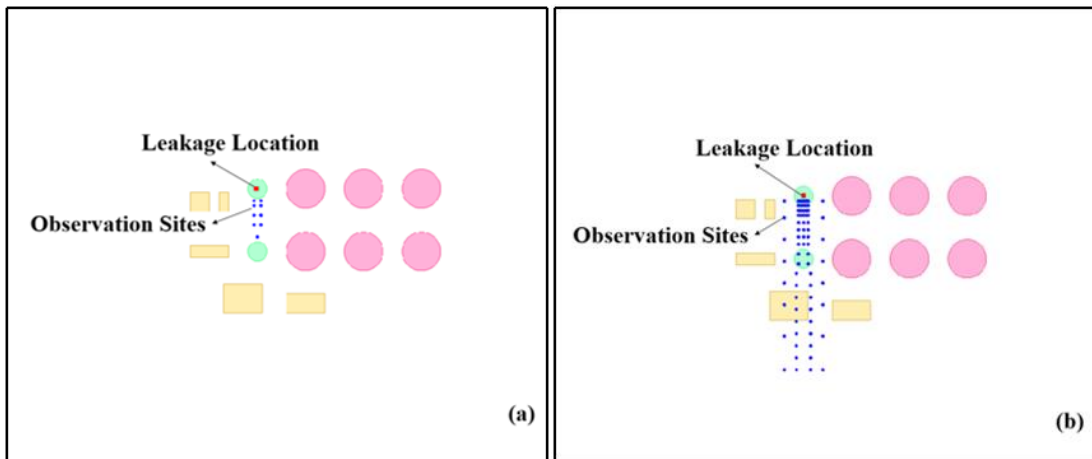


407

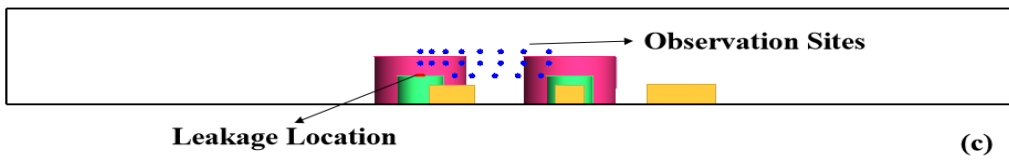
408

409

**Fig. 8.** The initial-guess leakage velocity ensemble used in the [CFD and EnKF coupling model](#)



410



411

412

413

**Fig. 9.** The layouts of the observation sites in three sections of the computational domain: (a) Z=20 m section, (b) Z=32 m section and (c) X=500 section

414

**Table 3** Configurations of the [CFD and EnKF coupling model](#)

Parameter	Setup value
-----------	-------------

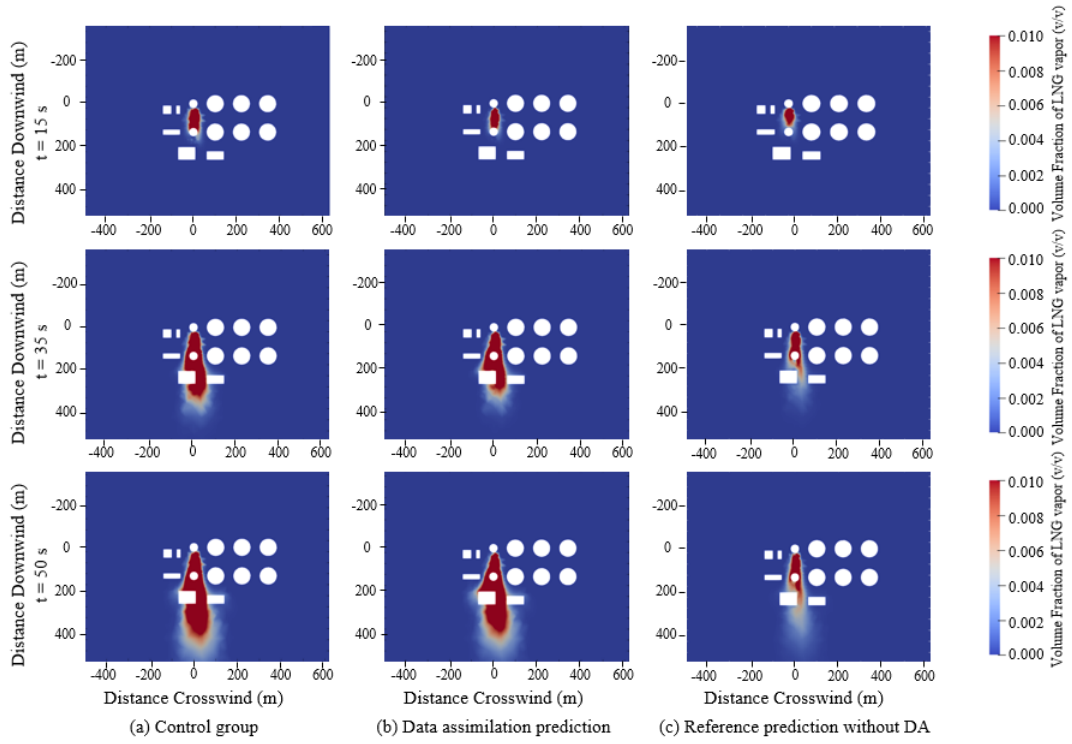
---

Ensemble number	120
Ensemble inflation	1.0
Number of measurement sites	100
Observation time interval (s)	0.5
Perturbation of velocity ensemble	$N(1, 0.1)$
Number of observation time steps	100

---

415 **3.3.2 Predictions of the CFD and EnKF coupling model**

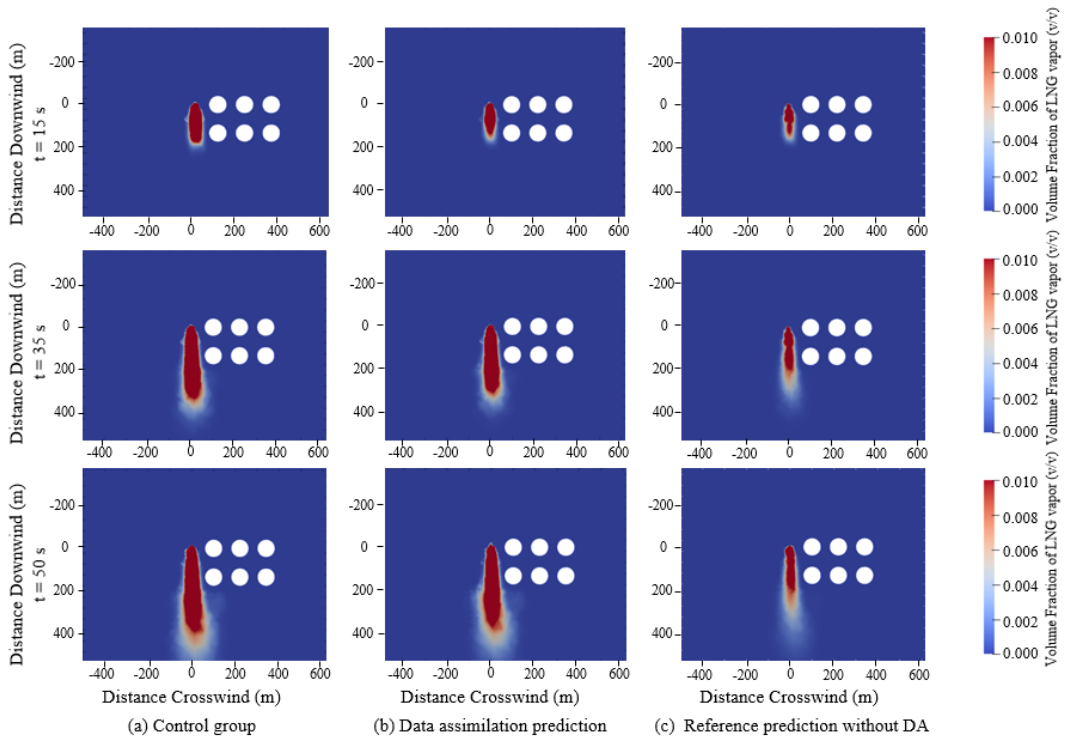
416 **Fig.10** to **Fig.12** illustrate the comparisons between the horizontal concentration  
417 distributions of the LNG vapor cloud at three different sections calculated by the control  
418 group, data assimilation group and a reference group without data assimilation (the  
419 leakage velocity in the this group was set as 5 m/s for reference). Moreover, we  
420 investigated the effectiveness of the proposed model by using three horizontal sections  
421 with different numbers of observation sites, 9 observation sites in the Z=20 m section,  
422 30 observation sites in the Z=32 m section and 0 observation sites in the Z=40 m section.



423

424

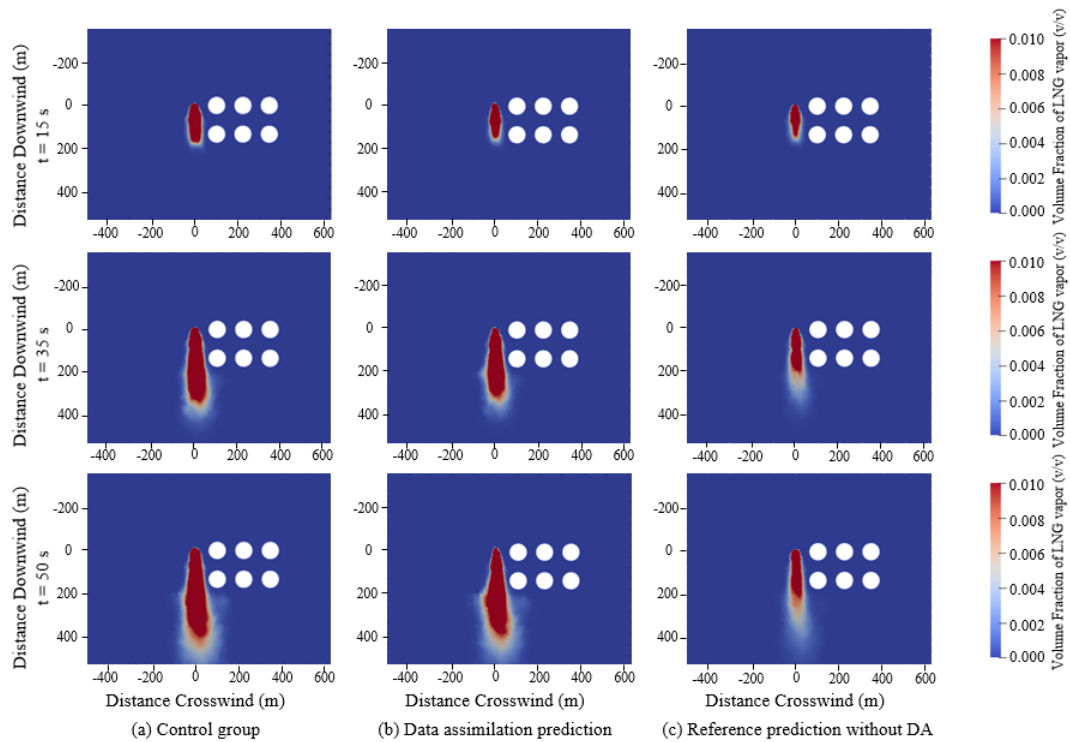
Fig.10 Horizontal concentration distribution of LNG vapor at Z=20 m section



425

426

Fig.11 Horizontal concentration distribution of LNG vapor at Z=32 m section



427

428

Fig.12 Horizontal concentration distribution of LNG vapor at Z=40 m section

429

The concentration distributions of LNG vapor at three different horizontal sections

430

calculated by three different simulation groups can be seen in **Fig.10** to **Fig.12**. At the

431

initial stage of vapor leakage and dispersion, there was no obvious difference of LNG

432

vapor distribution range area between the data assimilation prediction and the reference

433

prediction without DA due to the fact that the leakage velocity used in the two groups

434

was similar. The LNG vapor distributions in three sections of the control group were

435

slightly larger than the two predictions at 15 s because the underestimation of the

436

leakage velocity in two prediction groups led to the underestimation of the LNG vapor

437

distribution area. The correlation coefficients between the data assimilation prediction

438

and the reference prediction without DA and the control group distribution at the

439

observation sites are respectively 0.93 and 0.75 at 15 s. As time goes on, the difference

440 of LNG vapor distribution between the control group and the reference prediction  
441 without DA increased gradually because of the difference existing in the vapor leakage  
442 velocity. However, the data assimilation group obtained the LNG vapor distribution  
443 predictions with good similarities compared with the actual LNG vapor distribution in  
444 the control group at 35 s and 50 s, in which the correlation coefficients between the data  
445 assimilation prediction and the control group at the observation sites are 0.98 and 0.96  
446 respectively. Meanwhile, the correlation coefficient between the reference prediction  
447 without DA and the control group at the observation sites is only 0.48 in the end. That  
448 was because the observation data were used to correct the errors in the data assimilation  
449 prediction gradually and finally achieve the prediction of LNG vapor distribution with  
450 relatively high accuracy by the [CFD and EnKF coupling model](#). Additionally, the LNG  
451 vapor distribution predictions in the three sections calculated by the [CFD and EnKF](#)  
452 [coupling model](#) were all comparable to the actual distributions in the control group,  
453 which means that the [CFD and EnKF coupling model](#) could realize the correction of  
454 the LNG vapor distribution in the whole computational domain even in the section  
455 without observation site.

456 **Fig.13** presents the vertical concentration distribution of the LNG vapor cloud at  
457 X=500 m section calculated by the control group, the data assimilation group and the  
458 reference prediction group. The effectiveness of the proposed [CFD and EnKF coupling](#)  
459 [model](#) in the prediction of the LNG vapor vertical distribution could also be witnessed  
460 in **Fig.13**. After several data assimilation periods, the prediction of the LNG vapor



461 vertical distribution became more comparable to the actual distribution in the control  
462 group by using the [CFD and EnKF coupling model](#). The correlation coefficients  
463 between the data assimilation prediction and the control group at the observation sites  
464 in the X=500 m section are 0.99 at 35 s and 0.98 at 50 s, which means the observation  
465 data in the X=500 m section was utilized by the [CFD and EnKF coupling model](#)  
466 effectively. Whereas, the reference prediction without data assimilation was quite  
467 different from the actual distribution during the whole calculation period and with the  
468 correlation coefficient of -0.06 in the end.

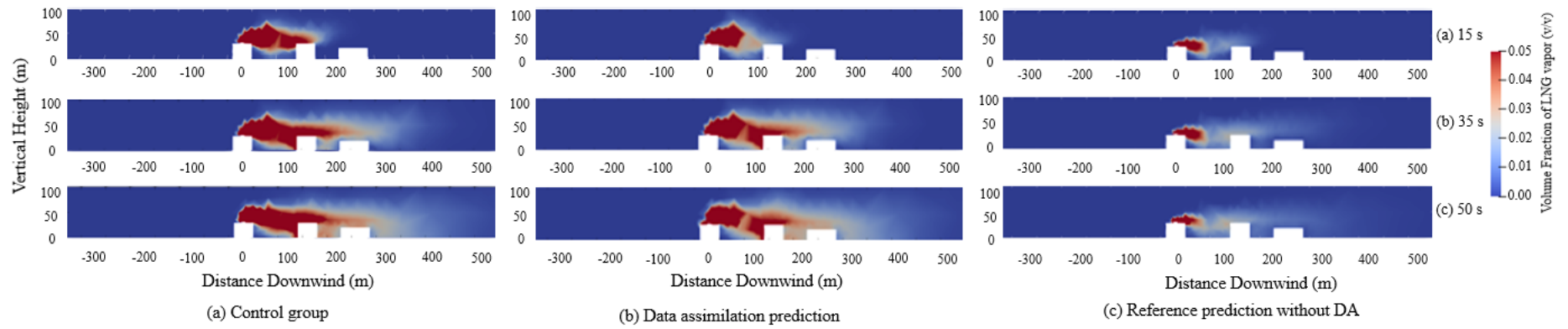


Fig.13 Vertical concentration distribution of LNG vapor at X=500 m section

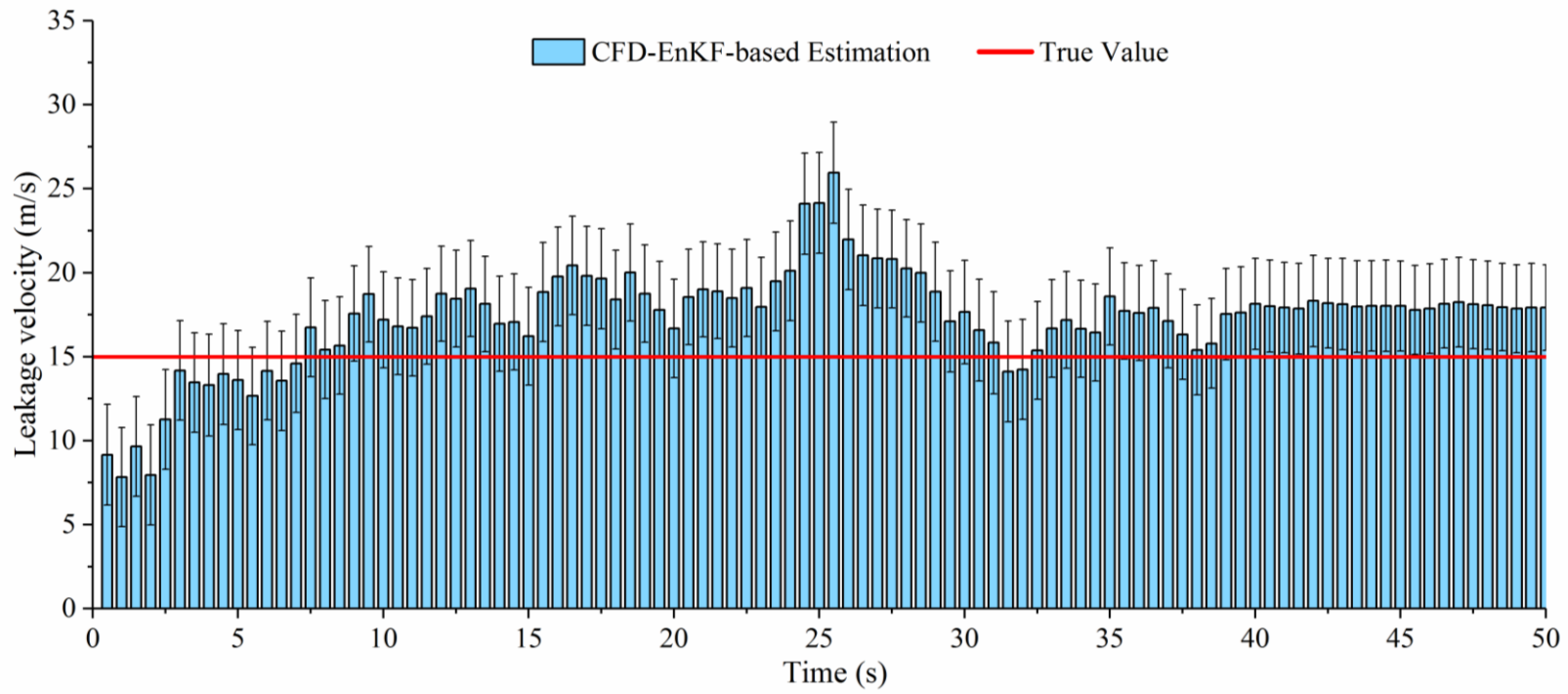


Fig.14 Leakage velocity estimation of the [CFD and EnKF coupling model](#)

459 **Fig.14** presents the leakage velocity estimation process of the LNG vapor at the  
460 leak hole by the proposed **CFD and EnKF coupling model**. The underestimation of  
461 leakage velocity can be seen at the initial period of time in **Fig.14**. That was because  
462 the underestimation existing in the initial-guess leakage velocity had some influence on  
463 the leakage velocity estimation and led to the errors of leakage velocity estimation at  
464 the initial several data assimilation periods. However, the overestimation of leakage  
465 velocity happened until around 30 s due to the overcorrection of the initial-guess  
466 leakage velocity caused by the data assimilation process. Finally, the estimation of  
467 leakage velocity became stable at around 18 m/s despite some fluctuations. The mean  
468 relative error between the leakage velocity estimation and the true value was 24.6 %  
469 from start to 30 s and the mean relative error of the leakage velocity estimation became  
470 16.1 % from 30 s to the end due to the estimation of leakage velocity became stable  
471 gradually after 30 s. Therefore, we come to a conclusion that the proposed **CFD and**  
472 **EnKF coupling model** could be used to provide a reasonable estimation of LNG vapor  
473 leakage velocity with a high similarity to the actual leakage velocity despite there are  
474 huge errors existing in the initial-guess leakage velocity.

#### 475 **4. Conclusion**

476 **In this paper, a three-dimensional CFD and EnKF coupling model was proposed**  
477 **with the combination of CFD simulation and data assimilation technique, which is of**  
478 **potentials to provide more accurate LNG vapor distributions and source term**  
479 **estimations for emergency response and safety control of LNG vapor leakage accidents.**

480 The main conclusions of this paper are presented below:

481 a) An OpenFOAM-based model was evaluated and validated in the simulation of  
482 LNG vapor leakage and dispersion by the Burro 8 spill test. The results show that the  
483 rhoReactingBuoyantFoam solver is effective in the simulation of LNG vapor dispersion  
484 compared with the experimental data and the ANSYS FLUENT results, which can be  
485 used as an alternative tool for simulating LNG vapor dispersion.

486 b) At the initial stage of LNG leakage, the process of LNG vapor dispersion in the  
487 LNG receiving terminal is dominated by the leakage velocity and the wind speed. Later,  
488 the natural wind velocity, buoyancy forces and the complex obstacle layouts will have  
489 a significant influence on the characteristics of the LNG vapor dispersion. The  
490 spreading features of the dense vapor driven by the wind field and the gravity can be  
491 well captured by the proposed CFD solver.

492 c) The proposed three-dimensional CFD and EnKF coupling model can obtain  
493 high-confidence prediction of spatiotemporal distribution of leaked LNG vapor and  
494 realize the reasonable estimation of LNG vapor leakage velocity. The effectiveness of  
495 the LNG vapor distribution predictions in the horizontal and vertical sections with  
496 different number of observation sites was evaluated with good reliability. Moreover, the  
497 estimation of leakage velocity can be obtained with acceptable errors after a period of  
498 data assimilation by the proposed model, which could be useful to provide leakage  
499 source information for decision-makers.

500 With the development and popularity of the supercomputer and the high-  
501 performance computing (HPC) technique, the computational efficiency of the proposed  
502 CFD and EnKF coupling model would be significantly improved, which helps to  
503 achieve a more timely source term estimation and LNG vapor distribution prediction.  
504 Additionally, machine learning is also a promising technique that can realize timely  
505 prediction of LNG vapor leakage and estimation of the leakage source by combining  
506 with the proposed model, which can be employed to generate huge data with high-  
507 confidence for model learning.

## 508 **Acknowledgements**

509 This work was supported by the National Key Research and Development Program of  
510 China (Grant No. 2017YFC0805001), the Beijing Nova Program (Grant No. 471  
511 Z201100006820072), the Yue Qi Young Scholar Program of China University of  
512 Mining & Technology, Beijing, and the Chinese Scholarship Council (Grant No:  
513 202006430007).

## 514 **References**

515 Baalisampanga, T., Abbassi, R., Garaniya, V., et al., 2019. Modelling an integra-  
516 ted impact of fire, explosion and combustion products during transitional ev-  
517 ents caused by an accidental release of LNG. *Process Safety and Environm-*  
518 *ental Protection*. 128,259-272.

519 Bengtsson L, Ghil M, Källén E. *Dynamic Meteorology: Data Assimilation Met-*  
520 *hods*. Springer New York 1981.

521 Burro Series Data Report, 1982. LLNL/NWC Report No.UCID-19075, v.1 2. B  
522 erkeley. CA: Lawrence Livermore National Laboratory.

523 Cormier, B.R., Qi, R., Yun, G., et al, 2009. Application of computational fluid  
524 dynamics for LNG vapor dispersion modeling: A study of key parameters. J  
525 urnal of Loss Prevention in the Process Industries. 22, 332-352.

526 Coyote Series Data Report, 1983. LLNL/NWC, UCID-19953. 1 2.

527 Dasgotra, A., Teja, G., Sharma, A., et al., 2018. CFD modeling of large-scale  
528 flammable cloud dispersion using FLACS. Journal of Loss Prevention in th  
529 e Process Industries. 56,531-536.

530 Falcon Series Data Report, 1990. Gas Research Institute, 1987 LNG Barrier Ve  
531 rification Field Trials, GRIReport No.89/0138, Chicago, IL.

532 Fiates, J., Vianna, S., 2016. Numerical modelling of gas dispersion using Open  
533 FOAM. Process Safety and Environmental Protection. 104,277-293.

534 Giannissi, S.G., Venetsanos, A.G., Markatos, N., et al., 2013. Numerical simulat  
535 ion of LNG dispersion under two-phase release conditions. Journal of Loss  
536 Prevention in the Process Industries. 26, 245-254.

537 Guo, D., Zhao, P., Wang, R., et al., 2019. Numerical simulation studies of the  
538 effect of atmospheric stratification on the dispersion of LNG vapor released  
539 from the top of a storage tank. Journal of Loss Prevention in the Process I  
540 ndustries. 61,275-286.

541 Ji, J., Tong, Q., Wang, L., et al., 2018. Application of the EnKF method for r  
542 eal-time forecasting of smoke movement during tunnel fires. Advances in E  
543 ngineering Software. 115,398-412.

544 Lee, C., Lim, Y., Han, C., 2012. Operational strategy to minimize operating co  
545 sts in liquefied natural gas receiving terminals using dynamic simulation. K

546       orean J. Chem. Eng. 29(4), 444-451.

547   Li, X.J., Zhou, R.P., Konovessis, D., 2016. CFD analysis of natural gas dispers  
548       ion in engine room space based on multi-factor coupling. Ocean Engineerin  
549       g. 111, 524-532.

550   Li, Y., Chen, X., Chein, M.H., 2012. Flexible and cost-effective optimization of  
551       BOG (boil-off gas) recondensation process at LNG receiving terminals. Ch  
552       emical Engineering Research and Design. 90, 1500-1505.

553   Lin, C.C., Wang, L., 2013. Forecasting simulations of indoor environment using  
554       data assimilation via an Ensemble Kalman Filter. Building and Environmen  
555       t. 64,169-176.

556   Liu, A.H., Huang, J., Li, Z.W., et al., 2018. Numerical simulation and experim  
557       ent on the law of urban natural gas leakage and diffusion for different buil  
558       ding layouts. Journal of Natural Gas Science and Engineering. 54, 1-10.

559   Luo, T., Yu, C., Liu, R., et al, 2018. Numerical simulation of LNG release an  
560       d dispersion using a multiphase CFD model. Journal of Loss Prevention in  
561       the Process Industries. 56,316-327.

562   Mack, A., Spruijt, M., 2013. Validation of OpenFoam for heavy gas dispersion  
563       applications. Journal of Hazardous Materials. 262, 504-516.

564   Ngodock H, Carrier M. A weak constraint 4D-var assimilation system for the  
565       navy coastal ocean model using the representer method// data assimilation f  
566       or atmospheric, oceanic and hydrologic applications (Vol. II). Springer Berli  
567       n Heidelberg 2013: 367-390.

568   Pontiggia, M., Derudi, M., Busini, V., et al., 2009. Hazardous gas dispersion: a  
569       CFD model accounting for atmospheric stability classes. J. Hazard. Mater.  
570       171, 739-747.



- 571 Pu, Z., Hacker, J., 2009. Ensemble-based Kalman filters in strongly nonlinear d  
572 ynamics. *Progress in Atmospheric Science*. 26(3), 373-380.
- 573 Qi, R., Ng, D., Cormier, B.R., et al, 2010. Numerical simulations of LNG vap  
574 or dispersion in Brayton Fire Training Field tests with ANSYS CFX. *J. Ha  
575 zard. Mater.* 183, 51-61.
- 576 Sklavounos, S., Rigas, F., 2006. Simulation of Coyote series trials—Part I: CF  
577 D estimation of non-isothermal LNG releases and comparison with box-mod  
578 el predictions. *Chemical Engineering Science*. 61, 1434-1443.
- 579 Siddiqui, M., Jayanti, S., Swaminathan, T., 2012. CFD analysis of dense gas di  
580 spersion in indoor environment for risk assessment and risk mitigation. *Jour  
581 nal of Hazardous Materials*. 209-210, 177-185.
- 582 Sun, B., Utikar, B.P., Pareek, V.K., et al, 2013. Computational fluid dynamics  
583 analysis of liquefied natural gas dispersion for risk assessment strategies. *Jo  
584 urnal of Loss Prevention in the Process Industries*. 26,117-128.
- 585 Valdes-Abellan, J., Pachepsky, Y., Martinez, G., 2018. MATLAB algorithm to i  
586 mplement soil water data assimilation with the Ensemble Kalman Filter usin  
587 g HYDRUS. *MethodsX*. 5,184-203.
- 588 Wu, J.S., Yuan, S.Q., Zhang, C., et al., 2018. Numerical estimation of gas rele  
589 ase and dispersion in coal mine using Ensemble Kalman Filter. *Journal of  
590 Loss Prevention in the Process Industries*. 56, 57-67.
- 591 Xing, J., Liu, Z.Y., Huang, P., et al., 2013. Experimental and numerical study  
592 of the dispersion of carbon dioxide plume. *Journal of Hazardous Materials*.  
593 256-257, 40-48.
- 594 Xue F., Kikumoto H., Li X., et al., 2018. Bayesian source term estimation of  
595 atmospheric releases in urban areas using LES approach. *Journal of Hazard*

596       ous Materials. 349,68-78.

597 Yuan, S.Q., Wu, J.S., Zhang, X.L., et al., 2019. EnKF-based estimation of natu  
598       ral gas release and dispersion in an underground tunnel. Journal of Loss Pr  
599       evention in the Process Industries. 62,103931.

600 Zhang, X., Huang M., 2017. Ensemble-based release estimation for accidental r  
601       iver pollution with known source position. Journal of Hazardous Materials.  
602       333,99-108.

603 Zhang, X., Li, J., Zhu, J., et al., 2015. Computational fluid dynamics study on  
604       liquefied natural gas dispersion with phase change of water. International Jo  
605       urnal of Heat and Mass Transfer. 91,347-354.

606 Zhang, X.B., Li, J.F., Zhu, J.K., et al., 2015. Computational fluid dynamics stu  
607       dy on liquefied natural gas dispersion with phase change of water. Internati  
608       onal Journal of Heat and Mass Transfer. 91, 347-354.

609 Zhang, X.L., Su, G.F., Yuan, H.Y., et al., 2014. Modified ensemble Kalman filt  
610       er for nuclear accident atmospheric dispersion: Prediction improved and sour  
611       ce estimated. J. Hazard. Mater. 280, 143-155.

612 Zhang, X.L., Li, Q.B., Su, G.F., et al., 2015a. Ensemble-based simultaneous em  
613       ission estimates and improved forecast of radioactive pollution from nuclear  
614       power plant accidents: application to ETEX tracer experiment. Journal of E  
615       nvironmental Radioactivity. 142,78-86.

616 Zhang, X.L., Su, G.F., Chen, J.G., et al., 2015b. Iterative ensemble Kalman filt  
617       er for atmospheric dispersion in nuclear accidents: An application to Kincai  
618       d tracer experiment. Journal of Hazardous Materials. 297,329-339.